

Poynting Vector Spin in Gyromagnetic Medium and its Impact on Backward Power Flow in Waveguiding Structures

Rajarshi Sen, *Graduate Student Member, IEEE*, Sarang Pendharker *Member, IEEE*

Abstract—This paper investigates the reactive power and spin of instantaneous Poynting vector in the bulk of gyromagnetic medium. It is shown that the gyromagnetic medium introduces a spin in the Poynting vector. The spin of the instantaneous Poynting vector and the relative strengths of the real and reactive power components are quantified using the Stokes plot method. Using this technique we investigate the presence of backward power propagation in a ferrite-filled waveguide. We present an analytical expression to locate the crossover point separating the forward and backward power propagation, where the real power propagation has a null. We further show how this backward power propagation leads to corresponding opposite surface currents on the waveguide plates of the ferrite-filled waveguide, while the potential difference between the two plates remain symmetric.

Index Terms—Gyrotropic medium, gyromagnetic medium, ferrites, Poynting vector, waveguide, surface wave.

I. INTRODUCTION

THE complex time-averaged Poynting vector (CTAPV) is an indicator of power flow and reactive power in a medium. Conventionally, while the complex form of CTAPV is important for the determination and extraction of the impedance of microwave networks, for propagative waves only the real part of the CTAPV is conventionally considered for investigation, as it corresponds to the average power flow. Recently, there has been a renewed interest in the general form of CTAPV with both its real and imaginary parts is again gaining importance for investigating the propagation of optical beams [1], the near field of Hertzian dipoles [2], evanescent waves [3], [4] and optical forces over particles [1], [5], [6]. These investigations involve using correspondence between the CTAP and the time-varying Instantaneous Poynting Vector (IPV).

The rotational aspect of IPV has been documented in the pioneering work of Halevi et al. [7], where they demonstrated elliptical trace drawn by the IPV for an inhomogeneous wave. In [8], Litvin demonstrated the relationship between complex CTAPV and elliptical rotation of the IPV in the case of Gaussian and Bessel beams. Litvin further highlighted how the rotational sense of the IPV is directly relevant to the divergence of the Gaussian and Bessel beams. Similarly, Mitri in [9] showed the rotation of the Poynting vector around a Poynting vector singularity generated by superposition of two coherent

opposite-handed vortex beams. In [10] Kim et al. related the reactive part of the complex CTAPV to the spinning nature of the IPV, in surface wave (SW) across a metamaterial-dielectric interface. Specifically, they emphasized the importance of the rotation of the IPV over transverse power transfer across the interface, thus explaining forward and backward power propagation across the dielectric-negative- ϵ interface. Even though wave propagation in gyrotropic medium has been thoroughly investigated, to the extent that it is now a text-book material [11]–[13], the methodology of using the complex CTAPV that captures the spinning nature of the IPV has not been thoroughly investigated in gyrotropic materials.

At microwave frequencies, gyromagnetic materials have been extensively used to realize isolators and circulators. In spite of gyromagnetic material based components becoming standard technology, several new designs and approaches are reported in recent years [14]–[19]. We see recent contributions to the theory of ferrite circulator designs [20]–[26] and phase sifters [27], [28] and isolators [29], [30]. Ferrite-based filters has also taken up recent research interest [31]–[33]. In [34], authors have proposed a design technique of a ultra-miniaturized ferrite patch antenna, which taps upon the potential of realizing ferrite-based devices with significant small footprint. In addition to radiating structures, the interesting scattering effects from cylindrical ferrite rods have also been subject to study [35]. Ueda et al. in [36] used the time-reversal asymmetry of ferrite material in conjunction with the space-inversion asymmetry of a ferrite-based metamaterial transmission to achieve variable phase-shifting nonreciprocity. In addition to these developments we also can see further interesting works related to gyromagnetic materials in the areas of topological devices [37], [38], magnonic spin waves [39]–[41], and mode-converting waveguides [42], [43].

The interest in gyrotropy based devices is also renewed by the enhanced capability to precisely engineer gyrotropic properties with composite materials [44]–[47]. In addition to supporting non-reciprocity [48], [49] gyromagnetic materials also exhibit hyperbolic isofrequency surfaces [50], [51], and can also be employed to control photonic spin [52] and enhance interconversion between microwave and optical fields [53]. In [52] we have investigated the effect of gyrotropy on supporting and suppressing different regimes of isofrequency surface topologies, the presence of material-locked photonic spin and its conflict with structure-induced photonic spin in a ferrite-filled waveguide. However, the understanding of the CTAPV and IPV in gyromagnetic media and in structures with

The authors are with the Electronics and Electrical Communication Engineering department, Indian Institute of Technology Kharagpur, Kharagpur, 721302 India (e-mail: sarang@ece.iitkgp.ac.in).

such gyromagnetic media has not been reported.

In this paper we investigate the CTAPV and rotating IPV

TABLE I
YIG FERRITE MATERIAL SPECIFICATIONS

Parameter	Specification
Magnetic saturation ($4\pi M_s$)	1820 Gauss
Magnetic bias (H_0)	3570 Oe
Lande factor (g)	2.02
Linewidth (ΔH)	18
Dielectric permeability (ϵ_f)	15
Dielectric loss tangent ($\text{tg}\delta$)	2×10^{-4}

for plane wave propagation in the bulk of a gyromagnetic medium. We show that for any arbitrary direction of propagation in such medium, the imaginary component of CTAPV is tangential to the isofrequency surface, while being normal to the direction of bias. The perpendicular nature of real and imaginary components of CTAPV results in spinning of IPV. To quantify the spin of IPV we propose Stokes parameter plot over Poincaré circle. Using these Stokes plots, we graphically represent the spin of the IPV across wave guiding structures with and without gyrotropic material. The Stokes plot analysis of such applications reveal the relation between the gyrotropy enforced modifications in the spin profile of the IPV and corresponding backward power propagation in the medium.

This paper is organized as follows: In section II, we investigate the complex CTAPV and time-varying IPV for bulk propagation in a gyromagnetic ferrite. In section III, we propose a simplified mechanism to quantify the spin of the IPV using the Stokes plot representation. We consider a

ferrite-filled waveguide in section IV and using the Stokes plot analysis we investigate the backward power propagation phenomenon and corresponding phenomena. In section V, we use the Stokes parameter plot to show the role of reactive power in supporting discontinuous power propagation across an air-ferrite interface supporting nonreciprocal SW propagation. Finally, we conclude with discussion in section VI.

II. POYNTING VECTOR IN BULK OF GYROMAGNETIC MEDIA

In order to investigate the nature of the Poynting vector in the bulk of gyrotropic media, we select YIG ferrite following the specifications given in Table I. YIG ferrite is one of the ferrite materials offering the least amount of gyromagnetic loss with $\Delta H = 18$ Oe. The standard permeability tensor for a \hat{z} -biased gyromagnetic ferrite is given as

$$\overleftrightarrow{\mu}_r = \begin{bmatrix} \mu' & -j\kappa' & 0 \\ j\kappa' & \mu' & 0 \\ 0 & 0 & 1 \end{bmatrix} \quad (1)$$

where the permeability term μ' and gyrotropy term κ' governs the wave propagation in the medium. This permeability tensor and all the mathematical formulations in this paper correspond to the basis function $e^{j(\vec{k}\cdot\vec{r}-\omega t)}$. Using this anisotropic permeability tensor, we can find the field intensities \vec{E} and \vec{H} in the material for propagating modes and derive the expressions for IPV and CTAPV (detailed derivation provided in the supplementary document). The expressions of IPV and CTAPV for wave propagating in $X - Y$ plane with $k_y = \text{are}$,

$$\begin{aligned} \vec{P}_{\text{IPV}} = H_0^2 k_0^2 & \left(\left(\frac{k_x(\epsilon_f k_0^2 \kappa'^2 (k_x^2 - \epsilon_f k_0^2)^2 + k_z^2 (k_x^2 + k_z^2 - \epsilon_f k_0^2 \mu')^2)}{2\omega\epsilon_0 (k_x^2 - \epsilon_f k_0^2)^2 (k_x^2 + k_z^2 - \epsilon_f k_0^2 \mu')^2} \right. \right. \\ & + \left. \frac{k_x(-\epsilon_f k_0^2 \kappa'^2 (k_x^2 - \epsilon_f k_0^2)^2 + k_z^2 (k_x^2 + k_z^2 - \epsilon_f k_0^2 \mu')^2)}{2\omega\epsilon_0 (k_x^2 - \epsilon_f k_0^2)^2 (k_x^2 + k_z^2 - \epsilon_f k_0^2 \mu')^2} \cos(2\omega t) \right) \hat{x} - \frac{\kappa' k_x (\epsilon_f k_0^2 - k_x^2 - k_z^2)}{2\omega\epsilon_0 (\epsilon_f k_0^2 - k_x^2) (k_x^2 + k_z^2 - \epsilon_f k_0^2 \mu')} \sin(2\omega t) \hat{y} \\ & + \left(\frac{k_z((k_x^2 + k_z^2 - \epsilon_f k_0^2 \mu')^2 + \epsilon_f k_0^2 \kappa'^2 (\epsilon_f k_0^2 - k_x^2))}{2\omega\epsilon_0 (\epsilon_f k_0^2 - k_x^2) (k_x^2 + k_z^2 - \epsilon_f k_0^2 \mu')^2} + \frac{k_z((k_x^2 + k_z^2 - \epsilon_f k_0^2 \mu')^2 - \epsilon_f k_0^2 \kappa'^2 (\epsilon_f k_0^2 - k_x^2))}{2\omega\epsilon_0 (\epsilon_f k_0^2 - k_x^2) (k_x^2 + k_z^2 - \epsilon_f k_0^2 \mu')^2} \cos(2\omega t) \right) \hat{z} \end{aligned} \quad (2)$$

$$\begin{aligned} \vec{P}_{\text{CTAPV}} = H_0^2 k_0^2 & \left(\frac{k_x(\epsilon_f k_0^2 \kappa'^2 (k_x^2 - \epsilon_f k_0^2)^2 + k_z^2 (k_x^2 + k_z^2 - \epsilon_f k_0^2 \mu')^2)}{2\omega\epsilon_0 (k_x^2 - \epsilon_f k_0^2)^2 (k_x^2 + k_z^2 - \epsilon_f k_0^2 \mu')^2} \hat{x} \right. \\ & + j \frac{\kappa' k_x (\epsilon_f k_0^2 - k_x^2 - k_z^2)}{2\omega\epsilon_0 (\epsilon_f k_0^2 - k_x^2) (k_x^2 + k_z^2 - \epsilon_f k_0^2 \mu')} \hat{y} + \left. \frac{k_z(\epsilon_f k_0^2 \kappa'^2 (\epsilon_f k_0^2 - k_x^2) + (k_x^2 + k_z^2 - \epsilon_f k_0^2 \mu')^2)}{2\omega\epsilon_0 (\epsilon_f k_0^2 - k_x^2) (k_x^2 + k_z^2 - \epsilon_f k_0^2 \mu')^2} \hat{z} \right) \end{aligned} \quad (3)$$

Here, $k_0 = \omega/c$ is the free space propagation constant, and c denotes the speed of light in vacuum. Interestingly, the IPV expression of Eq. (2) shows that in addition to the usual in-plane components along \hat{x} - and \hat{z} -directions, we have an additional gyrotropy-induced time-varying component along the transverse \hat{y} -direction. Moreover, we note that the time-varying transverse component of IPV is 90° out of phase compared to the in-phase time-varying x - and z -components as indicated

by their $\sin(2\omega t)$ and $\cos(2\omega t)$ dependencies. The 90° phase difference between the time-varying IPV components leads to a rotation of the IPV around the time-invariant component. This temporal rotation of the IPV is schematically illustrated in Fig. 1 (a) by blue elliptical conical trace around the time-invariant component of the IPV (equivalent to averaging in time) shown using the red arrow. The direction of rotation of the IPV around the time-invariant component is depicted

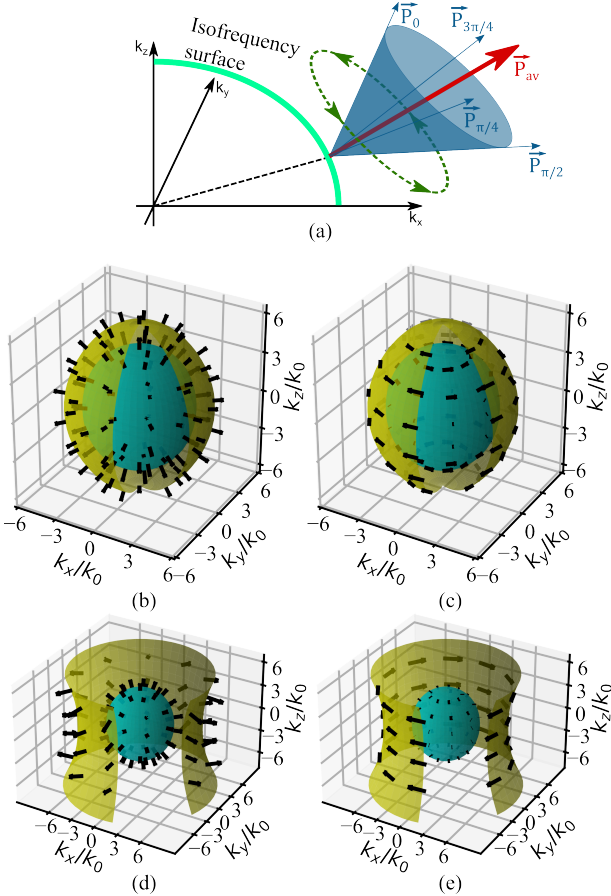


Fig. 1. (a) Graphical illustration of the time-varying behavior of the IPV. The real and imaginary components of the CTAPV over the 3D IFSs are shown in (b,c) corresponding to the elliptical regime at 7 GHz, and (d,e) corresponding to the hyperbolic regime at 11 GHz. Panels (b) and (d) correspond to the real part of the CTAPV and (c) and (e) correspond to the imaginary part.

using the green dashed curve having arrows encircling the trace, which is guided by the four time-phases ($\omega t=0, \pi/4, \pi/2$, and $3\pi/4$) of the IPV.

We observe that, the movement of the IPV follows an elliptical trace around the real part of CTAPV. This elliptical rotation depends on the additional transverse \hat{y} -component, which is usually not observed for a plane wave propagating in the bulk of a conventional non-gyrotropic material along the $X-Z$ plane.

To complete the investigation of power propagation in the bulk of the ferrite material, we look into the CTAPV in the medium. The CTAPV for plane waves in the bulk of the medium (see eq. 3) has a reactive power component along the transverse \hat{y} -axis in addition to the real part along the $X-Z$ plane of propagation. We can observe the correspondence between the CTAPV and IPV as the time-invariant in-plane components of the IPV being equal to the real part of the in-plane components of the CTAPV. Moreover, the out-of-phase time-varying transverse component of IPV equals the transverse reactive power component of CTAPV. This equality leads to the inference that the transverse reactive power component governs the transverse out-of-phase component of the IPV. In other words the complex CTAPV holds information about the

elliptical spin of the IPV around the time-invariant real power propagation. This transverse reactive power is an essential feature of the gyrotropic materials, as can be understood by the direct proportionality of the \hat{y} -component with the gyrotropic term κ . In the absence of gyrotropy, i.e. $\kappa' = 0$ will lead to the absence of the transverse reactive component of the complex CTAPV, and IPV instead of following an elliptical spin will follow a linear variation along the $X-Z$ plane. Additionally, reversing the bias orientation will lead to a sign change of κ' , which will lead to reversal of the phase of reactive power of the CTAPV and the sense of rotation of the IPV. Thus, the reactive power plays an essential role over the spin of the IPV in the gyrotropic medium.

Gyromagnetic ferrite can support different isofrequency surface (IFS) topologies based on the combinations of medium parameters μ' and κ' (as we showed in [52]). Accordingly, we select two difference frequencies, 7 GHz and 11 GHz, which supports the medium parameters necessary for the elliptical and hyperbolic IFS topologies, respectively. Investigating the Poynting vector corresponding to the elliptical and hyperbolic regimes of wave propagation gives us a comprehensive understanding of power propagation behavior in the gyromagnetic ferrite medium. Figure 1(b,c) and (d,e) show the real and reactive components of CTAPV across the IFSs in the elliptical and hyperbolic regimes, respectively. Panels (b) and (d) correspond to the real part of the CTAPV, and the imaginary part for the two regimes is shown in panels (c) and (e). We observe that the real part of CTAPV is normal to the IFS, which is in agreement with previous studies in the literature. However, we also observe the transverse nature of the reactive power component tangential to the surface, and transverse to the direction of propagation. This gyrotropy-induced reactive power in the transverse direction is an important property of wave propagation in the gyrotropic medium. It plays a crucial role in governing guided wave propagation involving gyrotropic materials (as we will see in sections IV and V). The results shown in Fig. 1 corresponding to the CTAPV was computed for a loss-less scenario. However, our investigation including standard material losses shows the negligible effect of the losses over the fundamental results reported in this work and are given in the supplementary document.

Conventional guided wave applications often contains a reactive part of in the CTAPV. Further, when a gyrotropic material inherently supporting reactive power for bulk modes is introduced to such applications, the combined effect has a strong impact over the power propagation characteristics of the guiding structure. To better understand the role of the reactive power over the overall power propagation, we propose a method of quantifying the spin of the IPV using the complex CTAPV in the next section.

III. QUANTIFICATION OF POYNTING VECTOR ROTATION USING STOKES CIRCLES

Considering wave propagation along \hat{x} -axis for a \hat{z} -biased ferrite, the medium can support a TEM and a TE mode propagation. The field components corresponding to these two propagation modes are (E_y, H_z) and (E_z, H_y, H_x) ,

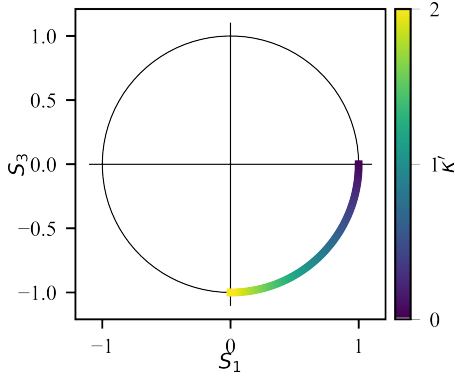


Fig. 2. Variation of Stokes parameters S_1 and S_3 over the Poincaré circle corresponding to the variation of κ' from 0 to 2. We have $\mu' = 2$ for this propagation scenario along \hat{x} -axis.

respectively. For the TE bulk mode, we can observe the additional longitudinal field component H_x supported by the medium, which has a 90° difference with respect to the transverse component. As a result the CTAPV has a longitudinal real $P_x = -0.5\text{Re}(E_z^* H_y)$ and a transverse reactive $P_y = 0.5\text{Im}(E_z^* H_x)$ power component. Using this CTAPV in the complex phasor form, we can quantify the spin of the IPV using the classical approach of computing the spin vector as $\vec{S}_p = \text{Im}(\vec{P}_{avg}^* \times \vec{P}_{avg})$. However, this spin vector computation is insufficient in capturing the important information about the relative difference in magnitude of the real $|P_x|$ and reactive $|P_y|$ power components.

In order to quantify both the spin of the IPV as well as the relative difference of magnitude between $|P_x|$ and $|P_y|$, we use the Stokes parameters $S_0 = |P_x|^2 + |P_y|^2$, $S_1 = |P_x|^2 - |P_y|^2$, $S_2 = 2|P_x||P_y|\cos\phi$, and $S_3 = 2|P_x||P_y|\sin\phi$. Here, S_0 correspond to the magnitude of the CTAPV. The S_2 parameter will be always zero for our TE mode of propagation as we have $\phi = 90^\circ$. The S_1 parameter gives us information about the relative difference between the magnitude of power components. The final parameter S_3 is equivalent to the conventional spin vector \vec{S}_p and gives information about spin of the IPV. Conventionally, these Stokes parameters can be traced over the Poincaré sphere. However, since we have $S_2 = 0$ in this case, we can represent the Stokes parameters over a 2D Poincaré circle which is normalized to the maximum radius of 1 by dividing S_1 and S_3 by S_0 at every gyrotropy value.

The propagation constant corresponding to the TE mode propagation along \hat{x} can be written as $k_x = k_0\sqrt{\epsilon_{eff}\mu_{eff}}$, where the effective permeability μ_{eff} is $\mu_{eff} = (\mu'^2 - \kappa'^2)/\mu'$. We consider the elliptical regime for the TE mode propagation which takes place when we have μ' as positive and $|\mu'| > |\kappa'|$. Selecting frequency of 7 GHz and $\mu' = 2$, we vary κ' from 0 to 2, which correspond to no-gyrotropy to the maximal gyrotropy that can sustain TE wave propagation in the elliptical regime before forcing k_x to be zero, triggering a gyrotropy-induced cutoff in the medium.

The corresponding Stokes plot with respect to variation in the κ' is shown in Fig. 2 where S_0 is normalized for the entire sweep of κ' making trace move along the unity perimeter of the Poincaré circle. We can observe that with increasing value

of κ' from 0 to 2, the Stokes plot moves from the coordinate $S_1 = 1, S_3 = 0$ to $S_1 = 0, S_3 = -1$ at which point the k_x becomes 0, leading to a gyrotropy-induced cutoff. From the point of view of the power components of the CTAPV, these two extreme points refer to the point where there is no reactive power (at the no-gyrotropy condition) and when the magnitude of real and reactive power is equal. Apart from the relative magnitude of the real and reactive power components, the S_3 parameter which increases with the κ' indicates the increase in the spin of the IPV, until it becomes circular before the cutoff. Thus, this Stokes plot representation is an effective tool in quantifying both the relative magnitude of the components of the CTAPV as well as the spin of the IPV, both of which are important for gyrotropic materials especially for waveguiding applications. In the next section, we shall look into the application of Stokes plot analysis corresponding to CTAPV in a ferrite-filled rectangular waveguide.

IV. GYROTROPY CONTROLLED POYNTING VECTOR IN FERRITE-FILLED WAVEGUIDE

We start our investigation with a benchmark scenario of a standard dielectric-filled non-gyrotropic rectangular waveguide of cross-sections $a = 5$ mm and $b = 3$ mm, as shown in Fig. 3(a). The parameters a , b and l correspond to the broad side dimension, narrow side dimension and length of the waveguide, respectively. The dielectric permittivity and permeability values are $\epsilon_r = 15$ and $\mu_r = 1.5$, respectively. Considering the fundamental TE_{10} mode, we find the longitudinal real and transverse reactive power components of the complex CTAPV as

$$P_x = \frac{0.5E_0^2 k_x \cos^2(k_y y)}{\omega\mu_0}, \quad P_y = \frac{0.25E_0^2 k_y \sin(2k_y y)}{\omega\mu_0} \quad (4)$$

Here, the $k_y = \pi/a$ is the cut-off wave number and the propagation constant is represented as $k_x = \sqrt{k_0^2\epsilon_r\mu_r - k_y^2}$. The plots corresponding to the P_x and P_y components across the dielectric waveguide at frequency of 7 GHz are shown in Fig. 3(b) and (c), respectively. We can observe the symmetric and anti-symmetric profiles of the real and reactive power components, respectively. Using these power components, we compute and show the Stokes plot in Fig. 3(d). S_1 and S_3 are normalized with respect to the maxima of S_0 along the cross-section. The location along the cross-section (y -axis) is color-mapped over the Stokes plot.

The Stokes plot representation for the dielectric-filled waveguide follows a cardioid pattern which is symmetric across the $S_3 = 0$ line. The segments below and above this line correspond to the negative and positive spin of the IPV. Further, the right and left region with respect to the $S_1 = 0$ line indicates the dominance of real power over reactive power and vice versa, respectively. If $|P_x| > |P_y|$ then S_1 is positive. In Fig. 3(e) we plot the Stokes plot at three different frequencies along the dispersion curve for the dielectric-filled waveguide, at ω_1 ($f_1 = 6.38$ GHz), ω_2 ($f_2 = 7$ GHz) and ω_3 ($f_3 = 9.4$ GHz). We observe that the stokes plot representation corresponding to ω_1 , which is near to cutoff frequency has maximum occupancy in the left side

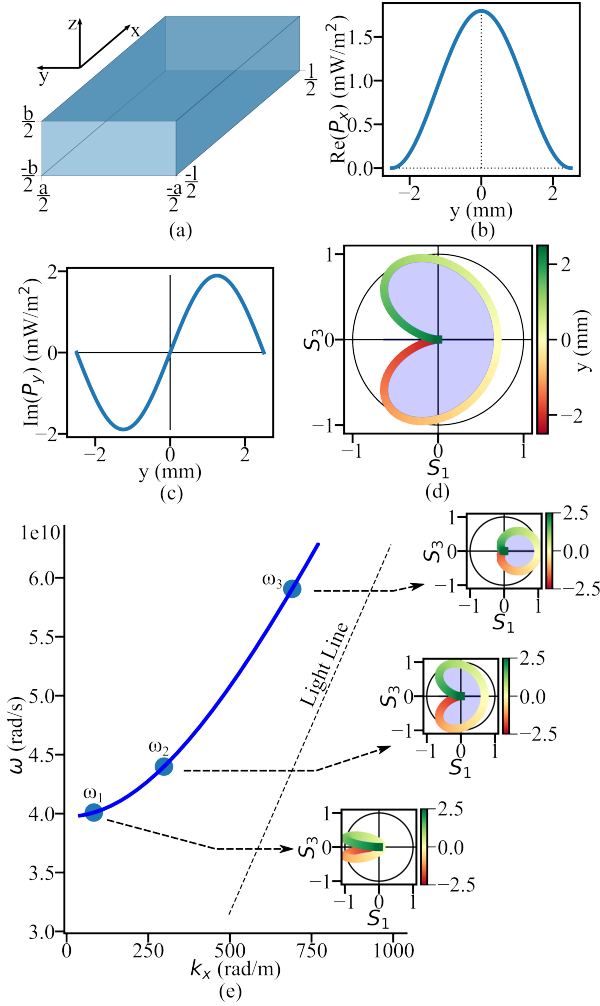


Fig. 3. (a) Geometry of the dielectric-filled rectangular waveguide. (b) Longitudinal real and (c) transverse reactive components of the CTAPV. (d) Stokes plot over the Poincaré sphere for wave propagation across the dielectric-filled waveguide at 7 GHz. (e) Dispersion curve corresponding to the dielectric-filled waveguide. Stokes plot representations at frequencies ω_1 ($f_1 = 6.38$ GHz), ω_2 ($f_2 = 7$ GHz) and ω_3 ($f_3 = 9.4$ GHz).

of $S_1 = 0$ line. Whereas, as we move away from the cutoff frequency, the Stokes plot shifts towards the right side of the $S_1 = 0$ line. Near the cutoff frequency the reactive power is maximum and real power diminishes. On the other hand, at higher frequencies, the rightwards shift of the Stokes plot indicates a relative increment of real power with respect to the imaginary power component along the cross-section. However, at all frequency points, the cardioid shape being symmetric across the $S_3 = 0$ line indicates equal and opposite photonic spin across the central axis of dielectric-filled waveguide at $y = 0$. The Stokes plot terminate at the origin of the Poincaré circle corresponding to $y = \pm a/2$, indicating that both real and reactive powers are zero at those points. Hence, Stokes plot in this benchmark scenario conveys a comprehensive understanding about the nature of IPV spin and relative magnitude of the real and reactive power components in the waveguide. With this reference, we can investigate the additional effect of the gyrotropy over the power propagation in a ferrite filled waveguide.

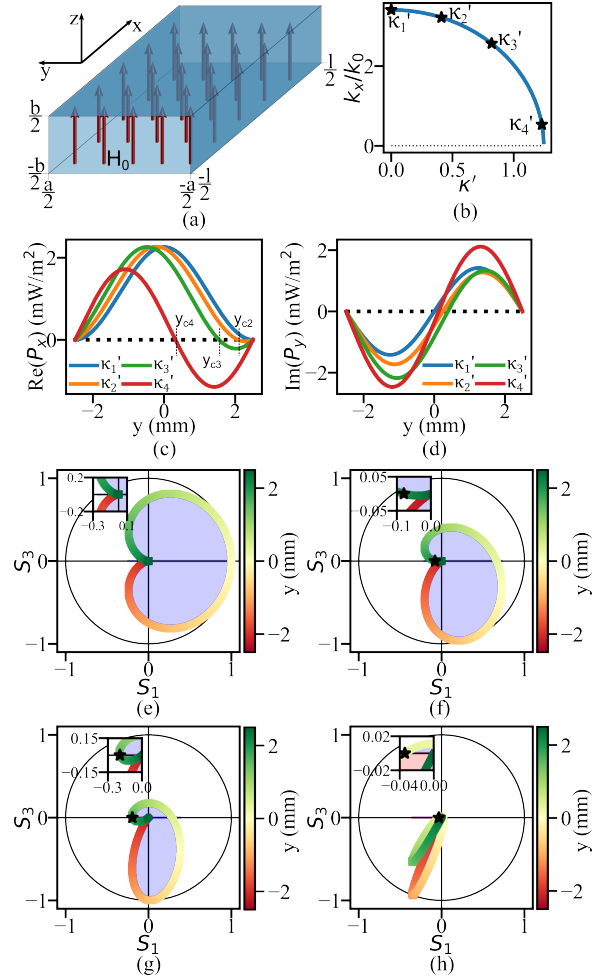


Fig. 4. (a) Schematic of a \hat{z} -biased ferrite-filled rectangular waveguide, (b) variation of k_x with respect to κ' variation from 0 to the maximum value before k_x reaches 0. Four gyrotropy values $\kappa'_1 = 0$, $\kappa'_2 = 0.41$, $\kappa'_3 = 0.82$, and $\kappa'_4 = 1.23$ are marked. (c) Longitudinal real and (d) transverse reactive components of CTAPV across the waveguide for the four gyrotropy values. (e)-(h) Stokes parameter plot across the cross-section of the waveguide for the four different gyrotropy values, respectively.

Figure 4(a) shows a rectangular waveguide filled with \hat{z} -biased YIG ferrite. The cross-section dimensions are selected as before ($a = 5$ mm and $b = 3$ mm). The cut-off wave-number in this case can be written as $k_y = \pi/a$. The propagation constant for the fundamental TE mode of the ferrite-filled waveguide is,

$$k_x = \sqrt{\left(k_0^2 \epsilon_f \frac{\mu'^2 - \kappa'^2}{\mu'} - k_y^2\right)}. \quad (5)$$

We consider the frequency of operation as 7 GHz and select $\mu' = 2$. With the help of eq. (5) we can see that for fixed value of k_y , when we increase the gyrotropy by increasing magnitude of κ' the value of the k_x decreases, and at some point before it reaches the value of μ' (maximum possible value for TE mode propagation in bulk of the ferrite medium), $k_0 \sqrt{\epsilon_f (\mu'^2 - \kappa'^2)}/\mu'$ becomes equal to $k_y = \pi/a$ leading to $k_x = 0$. Here, we get a gyrotropy-induced cut-off even when the medium supports the propagation of the bulk TE₁₀ mode. The variation of normalized k_x/k_0 with respect to

gyrotropy term κ' is shown in Fig. 4(b). For our selected material parameters and waveguide dimensions, the gyrotropy-induced cut-off is attained at $\kappa' = 1.245$.

For further investigation, we select four specific values of κ' . These gyrotropy points $\kappa'_1 = 0$, $\kappa'_2 = 0.41$, $\kappa'_3 = 0.82$, and $\kappa'_4 = 1.23$ are marked in Fig. 4(b). At the first point $\kappa'_1 = 0$ the material acts as non-gyrotropic, whereas at $\kappa'_4 = 1.23$ the gyrotropy is very near to the largest possible value before gyrotropy-induced cut-off is triggered in the waveguide. The field intensity equations for the TE₁₀ mode in the waveguide are

$$\begin{aligned} E_z &= E_0 \cos(k_y y) e^{jk_x x} \\ H_x &= j \frac{E_0 (\mu' k_y \sin(k_y y) - \kappa' k_x \cos(k_y y))}{\omega \mu_0 (\mu'^2 - \kappa'^2)} e^{jk_x x} \\ H_y &= - \frac{E_0 (\mu' k_x \cos(k_y y) - \kappa' k_y \sin(k_y y))}{\omega \mu_0 (\mu'^2 - \kappa'^2)} e^{jk_x x} \end{aligned} \quad (6)$$

We can compute the real P_x and imaginary P_y of the CTAPV \vec{P}_{avg} using these field equations. Figure 4(c) shows the longitudinal real P_x power component for the different values of κ' . We observe an important result: the gyrotropy leads to a decrease in the forward power propagation, and increase of an additional backward power flow region in the waveguide.

To develop a better understanding of this forward and backward power component, we analyze the expression for the CTAPV in eq. (6). The real component of CTAPV is computed as $\text{Re}(\vec{P}_{avg}) \cdot \hat{x} = -0.5 E_z^* H_y$, which leads to a multiplication between two functions of $(k_y y)$, i.e., $\cos(k_y y)$ and $\mu' k_x \cos(k_y y) - \kappa' k_y \sin(k_y y)$. Out of these two functions, the latter one is the reason for the backward power flow in the waveguide due to the offset of the H_y . If we have $\kappa' = 0$, the multiplication of these two functions is simplified as $\cos^2(k_y y)$ where there is no backward power component. Hence, the term $-\kappa' k_y \sin(k_y y)$ can be attributed as the source of the backward power. This second function also tells us the exact physical location, y_c , where $\text{Re}(P_x)$ makes a cross-over from forward to backward direction. Thus, we have the analytical expression for the power cross-over point as

$$y_c = \frac{a}{\pi} \tan^{-1} \left(\frac{\mu' k_x}{\kappa' k_y} \right), \quad (7)$$

This analytical eq. (7) is important from the device engineering point of view to locate the null of real power propagation along the cross-section of the waveguide. This equation also shows that for no-gyrotropy conditions $\kappa' = 0$, y_c shifts to $a/2$, which is at one of the walls of the waveguide. This position of y_c at the wall for $\kappa' = 0$ means there is no backward power flow, which is consistent with power propagation in standard dielectric waveguides. Note that for the three values κ'_1 , κ'_2 , and κ'_3 , we have marked three crossover points y_{c2} , y_{c3} , and y_{c4} , respectively, in Fig. 4(c). The transverse reactive power components $\text{Im}(P_y)$ for the four gyrotropy values are shown in Fig. 4(d). We can observe that the reactive power component maintains its sinusoidal variation at the extreme values of no gyrotropy ($\kappa'_1 = 0$) and strong gyrotropy ($\kappa'_1 = 1.23$). We can use these real and reactive power components for the difference κ' values to perform the Stokes plot analysis.

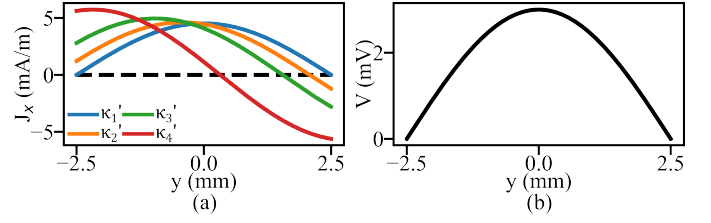


Fig. 5. (a) Longitudinal component of surface current density J_x at the top conducting plate ($z = b/2$) corresponding to gyrotropy values $\kappa'_1 = 0$, $\kappa'_2 = 0.41$, $\kappa'_3 = 0.82$, and $\kappa'_4 = 1.23$. Permeability term $\mu' = 2$ and frequency $f = 7$ GHz. (b) Potential difference V between the top and bottom conducting plates. E_0 is considered to be 1 V/m.

Figure 4(e)-(h) shows the variation of the Stokes parameter with respect to the cross-section of the waveguide for gyrotropy value of κ'_1 , κ'_2 , κ'_3 , and κ'_4 , respectively. For the first case of $\kappa'_1 = 0$ corresponding to the non-gyrotropic case, the Stokes parameter follows a symmetrical cardioid trace as was observed for the dielectric-filled waveguide. On the gradual increase of gyrotropy, we can see that most of the Stokes plot tends to shift to the lower half of the Poincaré circle. This primary occupancy of the lower half of Poincaré circle indicates the dominance of the negative S_3 , which results from the negative spin of the IPV enforced by the gyrotropic material. It is as if the gyrotropic material is dragging the Stokes plot in the negative S_3 region.

Further, we observe that as a result of the increase in the gyrotropy, the Stokes parameter plot makes an additional transition across the $S_3 = 0$ line from the $S_3 > 0, S_1 < 0$ to the $S_3 < 0, S_1 < 0$ quadrant before finally terminating at the origin at the end positions $y = +a/2$. It is interesting to observe that, this transition across the $S_3 = 0$ axis takes place precisely at y_c , and the rest of the Stokes plot beyond the additional transition in the $S_3 < 0, S_1 < 0$ quadrant corresponds to the backward power propagation, thus showing the relation between the enhanced negative IPV spin region with the backward power propagation. This Stokes plot segment beyond $y = y_c$ up to $y = a/2$ increases in magnitude with a corresponding increase in κ' , driving the cross-over point y_c towards the center $y = 0$ before the gyrotropy-induced cut-off is triggered. At the cut-off value of gyrotropy, both the lobes of the Stokes plot are divided in equal half by y_c . The existence of the the Stokes parameter almost completely in the $S_1 < 0, S_3 < 0$ quadrant at the cutoff condition indicates the dominance of the negative spin of the IPV and the magnitude of reactive power component with respect to the real power propagation. This understanding of the relation between additional spin of the IPV visualized by extended lobe of Stokes plot in the $S_1 < 0, S_3 < 0$ quadrant is important for controlling the amount of power propagating in the backward direction.

The backward power flow in the ferrite-filled waveguide is also related to the surface current density on the top and bottom conducting walls of the waveguide. We compute the longitudinal component of surface current density at the top conducting plate ($z = +b/2$) as $J_x = (\hat{z} \times \vec{H}) \cdot \hat{x}$ and plot it corresponding to four different gyrotropy values $\kappa'_1 = 0$,

$\kappa'_2 = 0.41$, $\kappa'_3 = 0.82$, and $\kappa'_4 = 1.23$ in Fig. 5(c). These computations were conducted considering $\mu' = 2$, and $f = 7$ GHz. We can observe the oppositely directed part of J_x with null points along y_c . An animation file has been provided as a supporting file showing the cross-section view of \vec{J} at the top plate of waveguide for $\mu' = 2$ and $\kappa' = 0.6$ for better visualization of the oppositely directed J_x in the region $(y_c \leq y \leq a/2)$. Further, the opposite propagation of J_x increases with increase of gyrotropy of the medium. This oppositely directed surface current density profile matches the oppositely directed real component of the CTAPV across the cross-over point y_c as shown in Fig. 4(c). Further, we can compute the potential difference between the top and bottom plates of the waveguides as $V = bE_z$. This potential difference V with respect to the transverse \hat{y} -axis is shown in Fig. 5(d). It can be seen that V is independent of the effect of gyrotropy. This leads to an interesting scenario where the ratio between V and J_x is nonuniform along the \hat{y} -axis rather than being constant. Furthermore, this gyrotropy-induced variation of J_x with respect to V is consistent with the nonuniform wave impedance Z_{wave} along the cross section of the waveguide.

$$Z_{wave}(y) = -\frac{E_z}{H_y} = \frac{\omega\mu_0(\mu'^2 - \kappa'^2) \cos(k_y y)}{k_x \mu' \cos(k_y y) - \kappa' k_y \sin(k_y y)} \quad (8)$$

Taking this facts into consideration, we see that in the region where the real power propagates ($y_c < y < a/2$) in the backward direction, Z_{wave} is negative and J_x points in the opposite direction too. Specifically at the cross over point y_c , we have $Z_{wave} = \infty$ and $J_x = 0$. When the direction of propagation reverses, y_c also shifts to the other side of the waveguide, meaning the point with $Z_{wave} = \infty$ and $J_x = 0$ is not same for two counter propagating waves. In general, we have nonreciprocal Z_{wave} and J_x across the cross-section. This may have important implications for port terminal behavior for the opposite propagation directions of such waveguides.

V. STOKES PLOTS OF SURFACE WAVE ALONG AIR-FERRITE INTERFACE

Electromagnetic SW propagation along the interface between two media has been extensively investigated in literature. Here, we look at the power flow and CTAPV associated with such propagation with the help of the Stokes plot. Figure 6(a) represents an interface between two mediums, namely medium-1 and medium-2. These two mediums exist in the regions $y \leq 0$ and $y \geq 0$, respectively. We consider medium-1 to be air for simplicity. To gain insight into the role of gyrotropy and IPV spin, we consider two cases. In the first case medium-2 is a non-gyrotropic material (we will call it Negative Permeability Material, NPM) with $\kappa' = 0$ and frequency-dependent μ' same as the ferrite material which support negative permeability in a specific frequency range. In the second case, medium-2 is considered as the $-\hat{z}$ -biased ferrite material. The choice of these two media is done to highlight the difference between the transverse reactive power, spin of IPV and oppositely directed real power propagation for non-gyrotropic and gyrotropic surface wave.

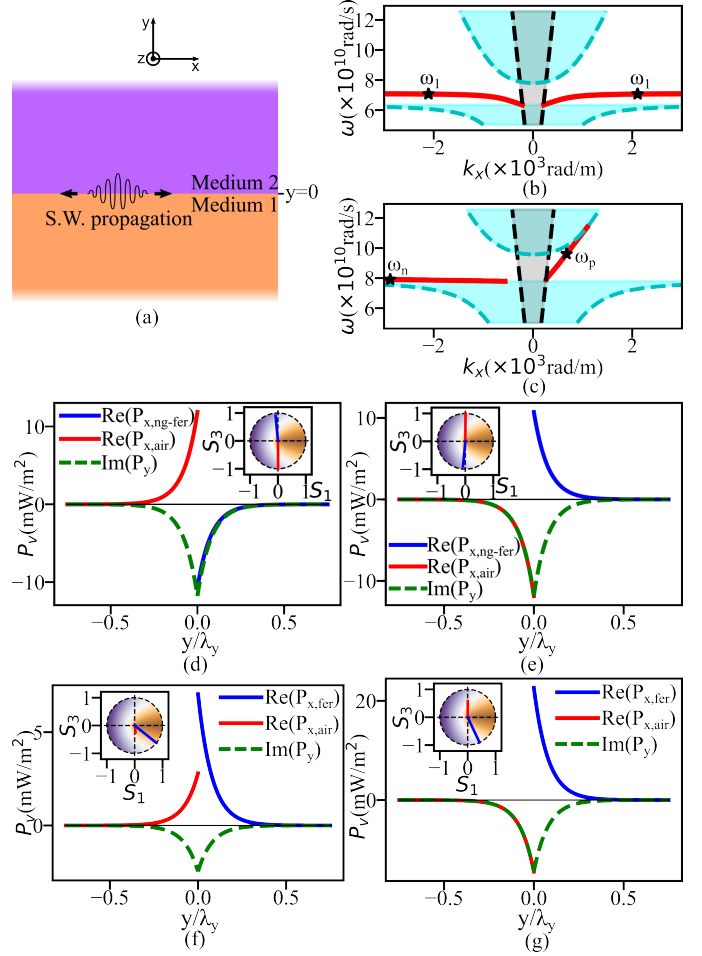


Fig. 6. (a) Schematic representation of an interface between two media supporting SW propagation. Medium 1 is considered to be air and Medium 2 is considered to be NPM material in the first case and $-\hat{z}$ -biased ferrite in the second case. (b) and (c) shows the dispersion plot corresponding to air-NPM and air-ferrite interfaces, respectively. Real and imaginary power components corresponding to air-NPM interface are shown in panel (d,e) and air-ferrite in (f,g). Further, (d) and (f) correspond to forward propagation, and (e) and (g) correspond to backward propagation. Stokes plot representation is added as insets to these plots with colormap representation of the reactive power component.

The material properties for the ferrite material are selected as given in Table I. For both the cases the dispersion relation and field equations can be found analytically and are presented in the supplementary document. The dispersion relation corresponding to the air-NPM and air-ferrite interfaces are shown in Fig. 6(b) and (c), respectively. The dispersion curves are represented using red solid lines. The gray and cyan shaded regions correspond to bulk propagation in air and ferrite media, respectively. In the first case of air-NPM interface, the surface waves are reciprocal. The real and imaginary components of CTAPV at a frequency of $\omega_1 = 2\pi \times 11.25 \times 10^9$ rad/s are shown in Fig. 6(d) and (e) for the forward propagating and backward propagating mode, respectively. The frequency point is selected such that the group velocity is almost zero. At this frequency the direction of real power flow along the interface is almost equal and opposite. However, it can be seen that the reactive power flow is continuous across the interface and

is transverse to the direction of SW propagation. In [8], it was argued that the transverse reactive power accounts for the backward power flow. When the dispersion curve flattens out with zero group velocity, the magnitude of backward power flow in NPM is equal and opposite to the forward power flow. The spin of Poynting vector in these two regions are shown as inset Stokes plot. It can be seen that the IPV spin of propagating SW is opposite in the two medium, and the sense of spin - in both the medium - reverses with the direction of propagation.

Figure 6 (f) and (g) shows the real and imaginary components of CTAPV for air-ferrite interface at frequencies $\omega_p = 2\pi \times 15.3 \times 10^9$ rad/s and $\omega_n = 2\pi \times 12.6 \times 10^9$ rad/s, corresponding to the forward and backward dispersion curve of the Fig. 6 (c). It can be seen that unlike air-NPM interface, in this case the real component of CTAPV in ferrite is positive for forward as well as backward SW propagation. The gyrotropy induced spin in IPV ensures that the spin in ferrite is always negative. Therefore the dispersion curve of backward propagating mode flattens out - with zero net power flow - at a lower frequency, while the dispersion curve of the forward mode does not flatten out and the net power flow and group velocity does not become zero. Therefore understanding the combined effect of gyrotropy induced IPV spin and the structure or geometry induced spin is important for understanding gyrotropic SW propagation and its non-reciprocal nature.

VI. CONCLUSION

We have analytically investigated the complex CTAPV in the bulk of gyromagnetic ferrite medium and showed the relation between the transverse reactive component and the spin of the IPV. We showed that even in bulk propagation in gyromagnetic medium there is a reactive component on CTAPV, which causes spin in IPV. We quantified this spin and the relative strength of the power components using the method of Stokes plot representation. Using this Stokes plot analysis we showed how under strong gyrotropy condition, the reactive power becomes equal in magnitude to the real power, leading maximum spin of the IPV and suppression of TE wave propagation in the ferrite medium. Non-gyrotropic waveguiding structures also exhibit transverse spin of IPV, which can also be characterized by computing Stokes plots across the cross-section of the waveguiding structures. In a ferrite-filled waveguide, there is a conflict in the gyrotropy induced IPV spin and the structure induced IPV spin. In ferrite-filled waveguide an additional lobe in the $S_1 < 0, S_3 < 0$ quadrant of the Poincaré circle is introduced which correspond to the backward power propagation in the structure. Further, we showed the unsymmetrical nature of surface currents in such waveguides and which is related to the non-uniform Z_{wave} along the transverse direction of the waveguide. These results establish important relationship between the spin of the Poynting vector and the backward power propagation in waveguiding structures involving gyrotropic materials. This understanding will be helpful in providing crucial design principles to realize novel tunable and nonreciprocal waveguiding

applications. Our results corresponding to the nonuniform nature of current density and wave impedance in a ferrite-filled waveguide can be used to realize spatially varying terminal behavior for nonreciprocal applications.

REFERENCES

- [1] X. Xu and M. Nieto-Vesperinas, "Azimuthal imaginary poynting momentum density," *Phys. Rev. Lett.*, vol. 123, p. 233902, Dec 2019.
- [2] P. Baumgartner, A. Masiero, C. Riener, and T. Bauernfeind, "Simulation based poynting vector description of the field regions for simple radiating structures," *Electronics*, vol. 11, no. 13, 2022.
- [3] M. Nieto-Vesperinas and X. Xu, "Reactive helicity and reactive power in nanoscale optics: Evanescent waves, kerker conditions, optical theorems and reactive dichroism," *Phys. Rev. Res.*, vol. 3, p. 043080, Oct 2021.
- [4] M. F. Picardi, M. Neugebauer, J. S. Eismann, G. Leuchs, P. Banzer, F. J. Rodríguez-Fortuño, and A. V. Zayats, "Experimental demonstration of linear and spinning janus dipoles for polarisation- and wavelength-selective near-field coupling," *Light: Science & Applications*, vol. 8, p. 52, Jun 2019.
- [5] M. Antognozzi, C. R. Bermingham, R. L. Harniman, S. Simpson, J. Senior, R. Hayward, H. Hoerber, M. R. Dennis, A. Y. Bekshaev, K. Y. Bliokh, and F. Nori, "Direct measurements of the extraordinary optical momentum and transverse spin-dependent force using a nanocantilever," *Nature Physics*, vol. 12, pp. 731–735, Aug 2016.
- [6] M. Nieto-Vesperinas and X. Xu, "The complex maxwell stress tensor theorem: The imaginary stress tensor and the reactive strength of orbital momentum. a novel scenery underlying electromagnetic optical forces," *Light: Science & Applications*, vol. 11, p. 297, Oct 2022.
- [7] P. Halevi and A. Mendoza-Hernández, "Temporal and spatial behavior of the poynting vector in dissipative media: refraction from vacuum into a medium," *J. Opt. Soc. Am.*, vol. 71, pp. 1238–1242, Oct 1981.
- [8] I. A. Litvin, "The behavior of the instantaneous poynting vector of symmetrical laser beams," *J. Opt. Soc. Am. A*, vol. 29, pp. 901–907, Jun 2012.
- [9] F. G. Mitri, "Superposition of nonparaxial vectorial complex-source spherically focused beams: Axial poynting singularity and reverse propagation," *Phys. Rev. A*, vol. 94, p. 023801, Aug 2016.
- [10] K.-Y. Kim, J. Kim, I.-M. Lee, and B. Lee, "Analysis of transverse power flow via surface modes in metamaterial waveguides," *Phys. Rev. A*, vol. 85, p. 023840, Feb 2012.
- [11] D. M. Pozar, *Microwave engineering*. Wiley; Fourth edition, India., 2012.
- [12] J. A. Kong, *Electromagnetic wave theory*. EMW Publishing, 2008.
- [13] A. Eroglu, *Wave Propagation and Radiation in Gyrotropic and Anisotropic Media*. Springer; New York., 2010.
- [14] Y.-K. Shi, B.-F. Wan, and H.-F. Zhang, "Nonreciprocal goos-hänchen effect at the reflection of electromagnetic waves from the one-dimensional magnetized ferrite photonic crystals," *Journal of Optics*, vol. 24, p. 055103, apr 2022.
- [15] H. Yan, L. Jing, J. Zhao, C. Niu, Y. Zhang, L. Du, and Z. Wang, "Broadband nonreciprocal spoof plasmonic phase shifter based on transverse faraday effects," *Opt. Express*, vol. 30, pp. 24000–24008, Jun 2022.
- [16] Y. Zhang, L. Jing, C. Niu, J. Zhao, and Z. Wang, "Broadband non-reciprocal gyromagnetic metasurface via magnetic kerker-type dimers," *Applied Physics Letters*, vol. 124, p. 231701, 06 2024.
- [17] B. Deng, H. Ding, P. Liu, Y. Xu, Z. Wu, T. Tian, C. Liu, and S. Zha, "Passive adaptive intensity high-pass devices for nonreciprocal hpm prevention," *IEEE Transactions on Microwave Theory and Techniques*, vol. 72, no. 10, pp. 5687–5698, 2024.
- [18] J. He, L. Zhang, L. Zhao, H. Mao, Q. Ba, Q. Luo, Y. Chen, H. Wu, and S. Liu, "Lattice kerker effect enabled single-layer nonreciprocal perfect absorbers by hybrid magnetic meta-atoms," *Opt. Lett.*, vol. 50, pp. 93–96, Jan 2025.
- [19] A. Grachev, S. Odintsov, E. Beginin, and A. Sadovnikov, "Nonreciprocal spin-wave transport in an asymmetric three-dimensional magnonic coupler," *Phys. Rev. Appl.*, vol. 21, p. 024031, Feb 2024.
- [20] M. M. M. Ali, M. Elsaadany, S. I. Shams, and K. Wu, "On the design of broadband asymmetric y-junction ferrite circulator for 60-ghz inter-satellite communication," *IEEE Transactions on Microwave Theory and Techniques*, vol. 72, no. 2, pp. 892–902, 2024.

- [21] V. Olivier, T. Monediere, B. Lenoir, H. Turki, C. Breuil, P. Pouliguen, and L. Huitema, "General coupling method for stripline ferrite circulators: Application on dual-band devices with complex central conductor shape," *IEEE Transactions on Microwave Theory and Techniques*, vol. 70, no. 7, pp. 3486–3497, 2022.
- [22] A. Ashley and D. Psychogiou, "Ferrite-based multiport circulators with rf co-designed bandpass filtering capabilities," *IEEE Transactions on Microwave Theory and Techniques*, vol. 71, no. 6, pp. 2594–2605, 2023.
- [23] M. M. M. Ali, S. I. Shams, M. Elsaadany, and K. Wu, "Stripline y-junction circulators: Accurate model and electromagnetic analysis based on gaussian field distribution boundary conditions," *IEEE Transactions on Microwave Theory and Techniques*, vol. 71, no. 1, pp. 146–155, 2023.
- [24] L. Marzall, D. Psychogiou, and Z. Popović, "Microstrip ferrite circulator design with control of magnetization distribution," *IEEE Transactions on Microwave Theory and Techniques*, vol. 69, no. 2, pp. 1217–1226, 2021.
- [25] V. Olivier, L. Huitema, B. Lenoir, H. Turki, C. Breuil, P. Pouliguen, and T. Monediere, "Dual-band ferrite circulators operating on weak field conditions: Design methodology and bandwidths' improvement," *IEEE Transactions on Microwave Theory and Techniques*, vol. 68, no. 7, pp. 2521–2530, 2020.
- [26] H.-T. Chou, C.-H. Chang, and Y.-T. Chen, "Ferrite circulator integrated phased-array antenna module for dual-link beamforming at millimeter frequencies," *IEEE Transactions on Antennas and Propagation*, vol. 66, no. 11, pp. 5934–5942, 2018.
- [27] A. Nafe and A. Shamim, "An integrable siw phase shifter in a partially magnetized ferrite ltcc package," *IEEE Transactions on Microwave Theory and Techniques*, vol. 63, no. 7, pp. 2264–2274, 2015.
- [28] S. Kagita, A. Basu, and S. K. Koul, "Characterization of ltcc-based ferrite tape in X-band and its application to electrically tunable phase shifter and notch filter," *IEEE Transactions on Magnetics*, vol. 53, no. 1, pp. 1–8, 2017.
- [29] F. A. Ghaffar, J. R. Bray, M. Vaseem, L. Roy, and A. Shamim, "Theory and design of tunable full-mode and half-mode ferrite waveguide isolators," *IEEE Transactions on Magnetics*, vol. 55, no. 8, pp. 1–8, 2019.
- [30] M. Nofresteri and T. Djerafi, "A tunable ferrite isolator for 30 ghz millimeter-wave applications," *IEEE Transactions on Magnetics*, vol. 57, no. 7, pp. 1–7, 2021.
- [31] M. Yang, H. Wang, F. M. Ghannouchi, T. Li, Y. Zhou, H. Li, Q. Li, L. Shi, M. Ou, R. Cheng, C. Fu, X. Liu, and B. Hu, "Design of filtering and limiting integrated ferrite device in high-power microwave electromagnetic environment," *IEEE Transactions on Microwave Theory and Techniques*, vol. 72, no. 7, pp. 3899–3907, 2024.
- [32] Q. Gao, L. K. Yeung, Y. Liu, A. Geiler, and Y. E. Wang, "Systematic design of planar millimeter-wave filters based on hexagonal barium ferrite (bam)," *IEEE Transactions on Microwave Theory and Techniques*, pp. 1–13, 2024.
- [33] M. Popov, Y. Xiong, I. Zavislyak, H. Chumak, O. Fedorchuk, S. Saha, R. Bidhanapally, H. Qu, M. R. Page, and G. Srinivasan, "Y-type hexagonal ferrite-based band-pass filter with dual magnetic and electric field tunability," *Scientific Reports*, vol. 13, p. 1179, Jan 2023.
- [34] S. Jemmeli, T. Monediere, E. Arnaud, and L. Huitema, "Ultra-miniature and circularly polarized ferrite patch antenna," *IEEE Transactions on Antennas and Propagation*, vol. 71, no. 8, pp. 6435–6443, 2023.
- [35] G. P. Zouros and K. Katsinos, "Em scattering by gyrotropic circular cylinders with arbitrarily oriented external magnetic bias," *IEEE Transactions on Antennas and Propagation*, vol. 71, no. 1, pp. 1174–1179, 2023.
- [36] T. Ueda, M. Kamino, T. Kondo, and T. Itoh, "Two-degree-of-freedom control of field distribution on nonreciprocal metamaterial-line resonators and its applications to polarization-plane-rotation and beam-scanning leaky-wave antennas," *IEEE Transactions on Microwave Theory and Techniques*, vol. 70, no. 1, pp. 50–61, 2022.
- [37] P. Zhou, G.-G. Liu, X. Ren, Y. Yang, H. Xue, L. Bi, L. Deng, Y. Chong, and B. Zhang, "Photonic amorphous topological insulator," *Light: Science & Applications*, vol. 9, p. 133, Jul 2020.
- [38] X. Xi, X.-M. Li, K.-P. Ye, H.-B. Wu, J. Chen, and R.-X. Wu, "Dual-polarization topological phases and phase transition in magnetic photonic crystalline insulator," *New Journal of Physics*, vol. 23, p. 083042, aug 2021.
- [39] C. M. Krowne, "Possibility of raising the frequency of rf limiters using the nonlinear spin wave–electromagnetic interaction in ferrites with high saturation magnetization," *IEEE Transactions on Microwave Theory and Techniques*, vol. 70, no. 4, pp. 2087–2097, 2022.
- [40] V. V. Tikhonov and A. N. Litvinenko, "Spin-wave diagnostics of the magnetization distribution over the thickness of a ferrite film," *Applied Physics Letters*, vol. 115, p. 072410, 08 2019.
- [41] S. Tang, M. S. Sarker, K. Ma, H. Yamahara, H. Tabata, and M. Seki, "Efficient spin-wave transmission in epitaxial thin films of defect spinel γ - $\text{Fe}_{2-x}\text{Al}_x\text{O}_3$," *Applied Physics Letters*, vol. 119, p. 082402, 08 2021.
- [42] A. Afshani and K. Wu, "Nonreciprocal mode converting waveguide and circulator," *IEEE Transactions on Microwave Theory and Techniques*, vol. 67, no. 8, pp. 3350–3360, 2019.
- [43] A. Afshani and K. Wu, "Generalized theory of concurrent multimode reciprocal and/or nonreciprocal siw ferrite devices," *IEEE Transactions on Microwave Theory and Techniques*, vol. 69, no. 10, pp. 4406–4421, 2021.
- [44] R.-L. Chern and Y.-Z. Yu, "Photonic topological semimetals in bigyrotropic metamaterials," *Opt. Express*, vol. 30, pp. 25162–25176, Jul 2022.
- [45] F. Zangeneh-Nejad, N. Kaina, S. Yves, F. Lemoult, G. Lerosey, and R. Fleury, "Nonreciprocal manipulation of subwavelength fields in locally resonant metamaterial crystals," *IEEE Transactions on Antennas and Propagation*, vol. 68, no. 3, pp. 1726–1732, 2020.
- [46] M. Li, N. Han, L. Qi, Y. Yan, R. Zhao, and S. Liu, "Topological transitions and topological beam splitters in gyromagnetic metamaterials," *Phys. Rev. B*, vol. 109, p. 085429, Feb 2024.
- [47] V. R. Tuz and A. B. Evlyukhin, "Magneto-plasmonic scattering by a disk-shaped particle made of an artificial dielectric," *Journal of Physics D: Applied Physics*, vol. 57, p. 135005, jan 2024.
- [48] C. Caloz, A. Alù, S. Tretyakov, D. Sounas, K. Achouri, and Z.-L. Deck-Léger, "Electromagnetic nonreciprocity," *Phys. Rev. Appl.*, vol. 10, p. 047001, Oct 2018.
- [49] M. I. Abdelrahman and F. Monticone, "Broadband and giant nonreciprocity at the subwavelength scale in magnetoplasmonic materials," *Phys. Rev. B*, vol. 102, p. 155420, Oct 2020.
- [50] V. I. Fesenko and V. R. Tuz, "Lossless and loss-induced topological transitions of isofrequency surfaces in a biaxial gyroelectromagnetic medium," *Phys. Rev. B*, vol. 99, p. 094404, Mar 2019.
- [51] V. R. Tuz and V. I. Fesenko, "Magnetically induced topological transitions of hyperbolic dispersion in biaxial gyrotropic media," *Journal of Applied Physics*, vol. 128, p. 013107, 07 2020.
- [52] R. Sen and S. Pendharker, "Gyrotropy-governed isofrequency surfaces and photonic spin in gyromagnetic media," *Phys. Rev. A*, vol. 105, p. 023528, Feb 2022.
- [53] D. Mukhopadhyay, J. M. P. Nair, and G. S. Agarwal, "Anti- \mathcal{PT} symmetry enhanced interconversion between microwave and optical fields," *Phys. Rev. B*, vol. 105, p. 064405, Feb 2022.